

Experimental methodology for measuring in-vacuum granular tribocharging

Cite as: Rev. Sci. Instrum. **90**, 125105 (2019); <https://doi.org/10.1063/1.5111983>

Submitted: 01 June 2019 . Accepted: 16 November 2019 . Published Online: 09 December 2019

D. Carter, and C. M. Hartzell 



[View Online](#)



[Export Citation](#)



[CrossMark](#)

ARTICLES YOU MAY BE INTERESTED IN

Production of highly charged ions of rare species by laser-induced desorption inside an electron beam ion trap

Review of Scientific Instruments **90**, 123201 (2019); <https://doi.org/10.1063/1.5128331>

Development of an interference-filter-type external-cavity diode laser for resonance ionization spectroscopy of strontium

Review of Scientific Instruments **90**, 123002 (2019); <https://doi.org/10.1063/1.5125307>

Radio frequency filter for an enhanced resolution of inelastic electron tunneling spectroscopy in a combined scanning tunneling- and atomic force microscope

Review of Scientific Instruments **90**, 123104 (2019); <https://doi.org/10.1063/1.5119888>



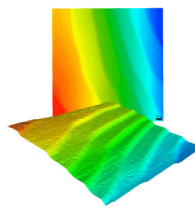
Nanopositioning
Systems



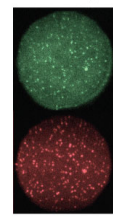
Modular
Motion Control



AFM and NSOM
Instruments



Single Molecule
Microscopes



Experimental methodology for measuring in-vacuum granular tribocharging

Cite as: Rev. Sci. Instrum. 90, 125105 (2019); doi: 10.1063/1.5111983

Submitted: 1 June 2019 • Accepted: 16 November 2019 •

Published Online: 9 December 2019



View Online



Export Citation



CrossMark

D. Carter^{a)} and C. M. Hartzell

AFFILIATIONS

Department of Aerospace Engineering, A. James Clark School of Engineering, University of Maryland, College Park, Maryland 20742, USA

^{a)}Electronic mail: d.p.carter4@gmail.com

ABSTRACT

We have developed an experimental methodology for measuring the charge distribution in granular mixtures due solely to particle-to-particle triboelectric charge exchange. Our experiment isolates the charging process from common influencing factors such as particle-to-container contact and atmospheric effects, creating conditions ideal for studying charge exchange on airless, dusty extraterrestrial bodies like the Moon and Mars. Charged grains are observed using high-speed videography as they fall through a uniform electric field, and their charge and size are characterized from their trajectories. This no-contact measurement method does not influence the charge and allows for the characterization of the overall distribution of charge by grain size in an arbitrary mixture. Our preliminary results indicate that charging measured with this test stand agrees well with computational charging models.

Published under license by AIP Publishing. <https://doi.org/10.1063/1.5111983>

I. INTRODUCTION

Charge transport in dielectric granular media has long been the subject of study by the electrostatic community. The separation of charge in granular mixtures due to triboelectric charging can cause dramatic and potentially dangerous electrical discharges in both natural^{1–4} and man-made^{5–8} granular mixtures and environments. Improving our understanding of this effect is critical for both ensuring safety of persons and equipment in highly charged environments and for utilizing this understanding to more efficiently conduct powder-handling operations such as electrospraying⁹ and pneumatic transport.^{5–8} Existing models for this process are limited, as the exact mechanism of charge transfer and the distribution of charge according to mixture properties remain uncertain. In part, this is due to the wide variety of possible candidates for charging mechanism and charge carrier among different materials, including trapped high-energy electrons,^{10–14} hydroxide ions or other adsorbed ions in the surface water layer,^{8,15–17} or broken polymer chains.¹⁸ The difficulty in obtaining detailed measurements of individual grain charge and charge distribution within the mixture while controlling for the environmental conditions necessary to isolate a particular charging mechanism makes a consistent predictive charging model especially elusive for dielectric grains.

Triboelectric charging is also believed to occur in the dusty surface layer of airless extraterrestrial bodies like the Moon. High-energy electrons from the solar wind plasma are deposited into this insulating dusty surface material, known as regolith. This charge may be readily exchanged when the surface is agitated in future manned or robotic surface operations. Not only is it important to accurately predict the magnitude and mechanism of this transfer to mitigate dangerous electrical discharge, we propose that this phenomenon may also be used as an electrostatic sieve, extracting both material components and size fractions from the regolith *in situ* for a variety of applications. Identifying an accurate tribocharging model for complex dielectric mixtures under high-vacuum conditions will be necessary to enable this application but is difficult to accomplish using existing techniques for tribocharging measurement.

II. EXISTING TECHNIQUES

Many common experimental tribocharging measurement techniques are unable to resolve individual grain charges or correlate precise grain sizes to the measured charge. Instead, techniques using charged probes^{12,19,20} or Faraday cups^{21,22} measure bulk charge polarity and/or magnitude of a particular subset of the tribocharged

sample and then measure the size distribution of that subset. These methods are useful in measuring the degree to which charge is segregated by size, but do little to characterize the magnitude of that charge or its distribution within particular regions of the size distribution.

Another common limitation of existing experimental methods is the mechanism by which grains are charged. Some experiments fail to control for particle-to-container charging, causing the charge distribution to be significantly less representative of particle-to-particle charging, particularly when the container is made of a different material.^{1,21,22} In other cases, to avoid particle-to-container charging, the mixture is agitated by fluidization with a gas, sometimes air^{1,21–24} or a presumably neutral gas like nitrogen^{12,20,25,26} or helium²⁷ to avoid influencing the charging process. However, experiments have suggested that the ambient atmosphere plays a large role in the magnitude and mechanism of charge separation, even for gases such as helium and nitrogen.²⁷ Although little data exist on whether this influences the direction or relative distribution of charge within the mixture, it is known that the humidity of the ambient atmosphere does affect the charging process.^{8,15–17}

There are experimental methods that provide the ability to correlate charge with grain size in a noninvasive way,²³ but many still use charging methods that are influenced by atmospheric effects. We have adapted the high-speed videography methodology described by Waitukaitis and Jaeger²³ to conduct the tribocharging process in vacuum, minimizing the effects of container contact and atmospheric influence on the charging process. This method sends falling charged particles through a uniform electric field and observes their trajectories from a comoving camera. As the experiment is conducted in vacuum, the effects of air resistance are eliminated, leaving only gravity and the electric force to act on the grains.

Our experiment differs from that of Waitukaitis and Jaeger in a few key ways. Primarily, the grains are kept in high-vacuum conditions throughout the charging and measurement processes. Although our operational pressure is not low enough here to ensure total elimination of adsorbed water from the atmosphere, we mitigate the effect of humidity by keeping the chamber sealed and under vacuum when not in use, storing the grains in a sealed container with desiccant packs, and maintaining an overall low-humidity laboratory environment. Future efforts could also include using lower pressures and/or preliminary high-vacuum baking of the grains before experimentation.

Additionally, we have designed our measurement and analysis software to measure individual grain diameters, rather than simply identifying large vs small grains, to work for arbitrary size distributions. Although this experimental test stand was designed with silica beads on the 10^{-4} meter scale, it is applicable to a variety of granular mixtures with arbitrary size distributions with diameters upwards of 10^{-5} m or even smaller with the use of higher magnification lenses. This also allows us to investigate the charging of complex mixtures like lunar regolith simulant.

III. EXPERIMENTAL PROCEDURE

For the purposes of this paper, we will consider a sample mixture of zirconia-silica ($\text{ZrO}_2:\text{SiO}_2$) beads from Glenn Mills, Inc.

Silica is known to undergo strong triboelectric charging and is the primary component of JSC-1A lunar regolith simulant. An accurate model for how zirconia-silica charges with itself will provide a strong foundation for a regolith charging model. The sample mixture used consists of 40 g each of two sizes of beads, with radii sieved to $100 \mu\text{m} \leq R_1 \leq 200 \mu\text{m}$ and $200 \mu\text{m} \leq R_2 \leq 300 \mu\text{m}$. Note that the two sizes used are not from the same fabrication batch and that subtle differences between them may contribute to charge exchange. Although this has significant implications for the accuracy of our modeling, the results of the experiment still validate the experiment's effectiveness as a measurement tool.

A. Physical setup

A photograph of the experimental apparatus is shown in Fig. 1(a). The interior of a small cylindrical stainless steel canister is coated with a polyurethane glue and covered with a thin layer of the granular mixture to be studied. This ensures that when shaken, the grains will have no contact with the container walls and charge exchange will only occur between grains of the mixture.²³ The canister is mounted on the shaker [Fig. 1(b)], aligned with the plates, attached to the motor, and clamped down. This shaker is a Pyle PLPW6D 600 W speaker and is powered through vacuum feedthroughs by a separate amplifier. The apparatus is then placed in a $30'' \times 24'' \times 24''$ vacuum chamber, connected to the multipin electrical feedthroughs and a separate high-voltage feedthrough for the electrodes, and pumped down to our operating pressure of $30 \mu\text{Torr}$. The side of the apparatus that faces the turbopump inlet is covered in a sheet of aluminum, ensuring that deflected grains cannot bounce into the turbopump during operation.

When the chamber has been evacuated to the desired pressure, the shaker can be activated. The canister is vigorously shaken vertically at 20 Hz for 5 min, thoroughly mixing the grains and causing them to tribocharge. Once the grains are charged, the camera is turned on and the electrodes are charged to their operating potential of 4000 V [Fig. 1(d)]. The electrodes are each 110 mm wide, 400 mm tall, and spaced 60 mm apart. Our camera is a PCO Dimax CS3 high-speed camera with a 1:1 macrolens. We record videos at 1000 frames/s at a resolution of $11 \mu\text{m}$ per pixel. These settings were chosen to maximize the frame rate for blur reduction and trajectory length while ensuring sufficient illumination for resolving the images. The grains are illuminated by two banks of light-emitting diode (LED) strips mounted on either side of the camera. Due to the compact nature of our test stand, there is limited available space for mounting lights; the lens and closely spaced electrodes obscure the grains from most directions. While the LED strips do provide sufficient illumination to identify and size grains to reasonable accuracy, a solution that provides additional illumination would dramatically improve this accuracy.

Data collection is an automated process controlled through LabVIEW. First, the grain release motor turns the lid of the canister 90° , revealing an aperture 5 mm in diameter through which a narrow stream of grains falls. As soon as the motor stops, the camera's chosen video settings are applied and the LED bank is turned on. The camera then begins recording and the electropermanent magnet [Fig. 1(c)] holding it at the top of the chamber is deactivated. The camera falls for just under half of a second and is

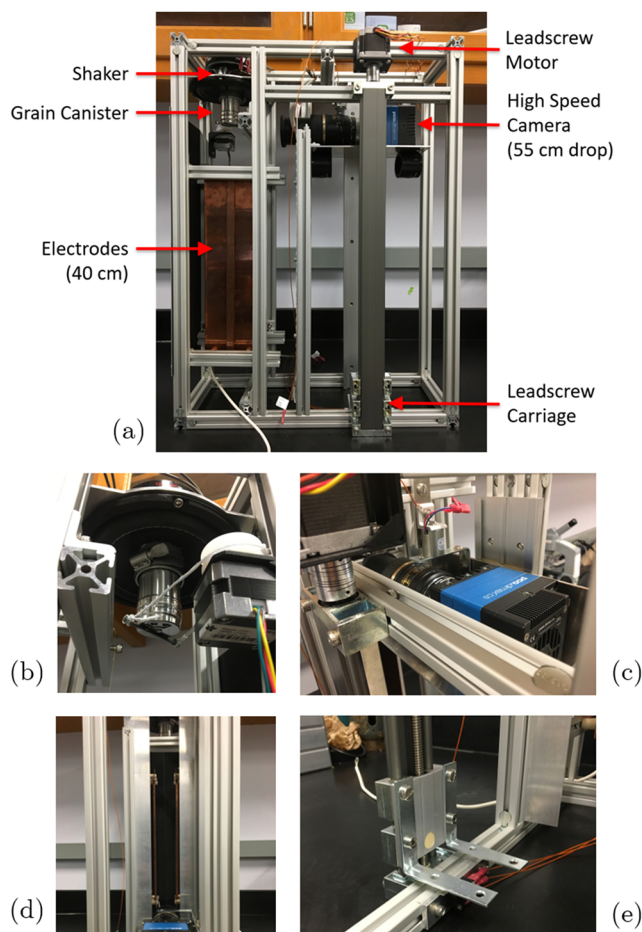


FIG. 1. (a) Experimental setup. The device is designed to be placed in a vacuum chamber and operated at high vacuum. Grains in the canister are tribocharged by the shaker and dropped through a region containing a transverse electric field. The camera is dropped and records the trajectories of the grains while both are in free fall. (b) Samples are extracted by activating a motor to rotate the canister lid. (c) The camera is held at the top of the device by an electropermanent magnet, which releases the camera carriage when a sample is released. (d) The grains fall between a pair of charged copper electrodes, causing them to accelerate laterally, and their trajectories are recorded by the camera. (e) A forklift carries the camera carriage back to the top, where it is again secured to the electropermanent magnet.

decelerated by rubber bumpers at the bottom of the camera carriage. One second after recording is started, the LEDs are turned off, recording is ceased, and the grain release motor reverses to close the canister again. Image buffers in the camera's onboard memory are read out into a binary file, and the image dimensions are stored to allow the data to be read out into images at a later time. The camera and high voltage electrodes can be powered down at this time, and the data are then reformatted into individual images.

For each granular mixture, multiple videos are taken to create a representative sample of the mixture. The camera is returned to the top of the device without breaking vacuum by means of a forklift traversing a leadscrew [Fig. 1(e)]. Two limit switches, one physical

switch at the bottom and one electrical switch completed through contact with the electropermanent magnet at the top of the chamber, resolve the carriage and forklift positions. A separate LabVIEW program automates this return, raising the forklift until the camera is secured at top and then lowering the forklift until it is flush with the bottom of the device. The forklift's resting position is low enough that the compression of the bumpers on the falling camera carriage does not cause the carriage to impact the lift.

IV. DATA PROCESSING AND ANALYSIS

A. Image filtering and grain identification

Figure 2 shows a sample video frame obtained by applying a noise-reduction filter to the raw data. The method we use for identifying and tracking particles was developed by Crocker and Grier.²⁸ We apply a bandpass filter to identify objects of a specified size, which we will refer to as a “standard diameter.” For the sample mixture discussed here, grains have diameters ranging between 100 and 300 μm , so we use a standard diameter of 25 pixels or approximately 280 μm . This value was chosen because the algorithm works best when the standard diameter is only slightly larger than the objects

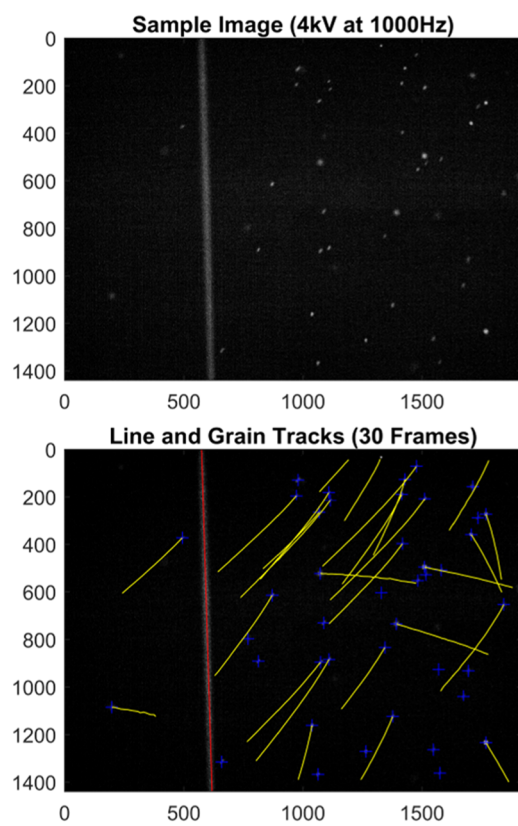


FIG. 2. Sample frame, with and without features overlaid. (Top) The noise-reduced frame alone. (Bottom) The same frame with grain locations (blue crosses) and string center (red line) identified. Grain trajectories (yellow arcs) are shown for the 30 frames following the one shown. Units are in pixels.

to be found, and the distribution of observed grain sizes trails off at approximately $270 \mu\text{m}$. After applying this filter, the result is then rescaled to a value out of 255.

Two prominent features remain in the filtered image: the alignment string and the grains themselves. To find the string, we locate its center on the image's central horizontal row of pixels and then move toward the top and bottom of the image, estimating the center along each row of pixels. These locations are used to calculate a linear fit to the string, providing a reference to the camera's minute variations in roll and yaw as it falls. The grains are found by identifying all local brightness maxima within a radius of a standard diameter. These estimated centers are refined by finding the centroid of the pixel values in the vicinity of each point. This reduces the influence of residual noise or asphericity on the identified center but can cause additional errors when two grains overlap or collide.

B. Trajectory determination

The grains are accelerated laterally by the electric field, and many also have some small nonzero vertical velocity relative to the camera. The trajectories formed by these grains from image frame to image frame can be analyzed to determine the charge-to-mass ratio of each grain. To construct these trajectories from the raw image data, we find the least-mean-square displacement of all pairings of grains with their nearest neighbors across each pair of frames, assigning a unique track number to each set of positions. From the sample video described in Sec. III, this process identifies 402 trajectories, many of which are simply individual unpaired grains; 125 of

these contain at least 10 frames, for which the average length is 42 frames.

The filters in Sec. IV A have a tendency to miss a small percentage of the grains that do not meet the brightness threshold, causing some tracks to be divided in two or more segments. This is exacerbated in the later frames as grains gain speed and may move so fast that their motion between frames exceeds the maximum for tracking. These effects inflate the number of valid trajectories found. Furthermore, while actual collisions between grains appear to be rare, close crossings do happen on occasion. When they do, only the brighter grain is identified and one trajectory sometimes incorrectly continues with the wrong grain. Even if these events are correctly flagged and rejected, the remaining tracks are primarily incomplete, and it is advantageous to manually inspect and correct them to obtain accurate trajectories.

We have developed an interface for examining and manually correcting trajectories by adding or removing grains, searching for grains that were missed due to overeager filtering, and deleting poorly resolved objects like overlapping grains or residual background noise. Each track is presented as a set of connected points, as in Fig. 3. The user can navigate from frame to frame using the "Prev Frame" and "Next Frame" buttons, and each grain location is presented in each frame as a candidate to be added, removed, or deleted using the corresponding buttons. In addition, the interface allows for manually selecting regions that clearly contain grains that were not identified by right-clicking. These grain locations can be added back to the frame, enabling the reconstruction of long grain tracks that would have otherwise been lost. With this

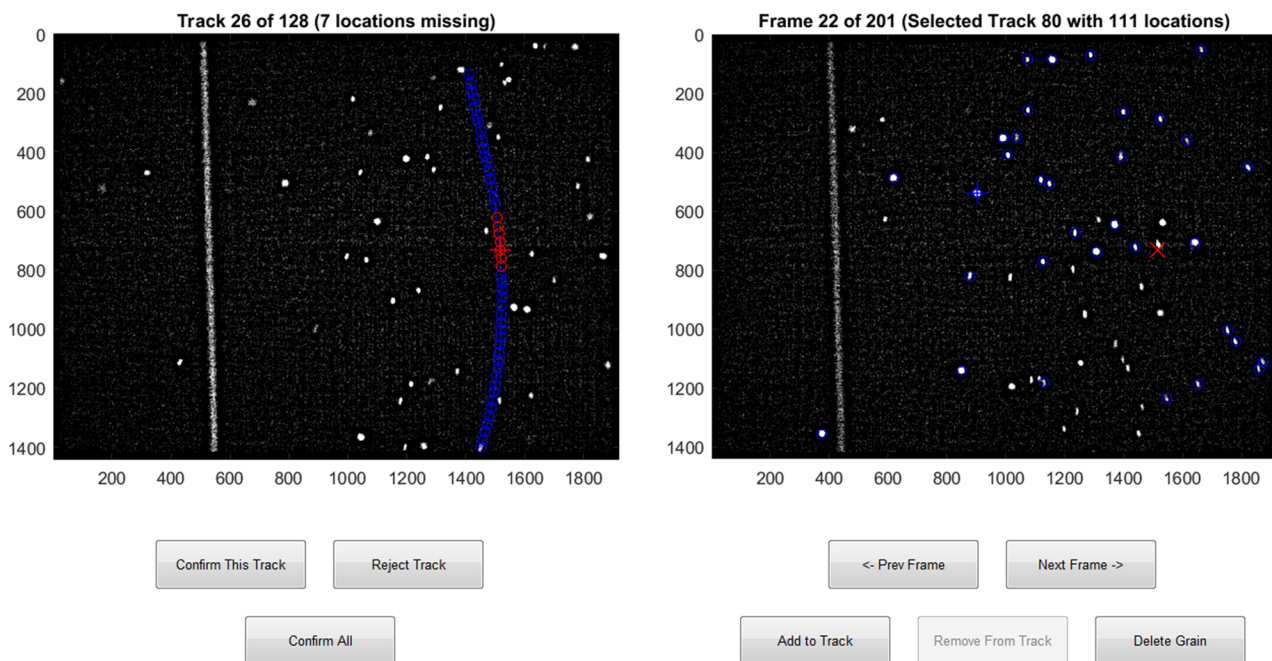


FIG. 3. Interface for editing tracks found by the tracking algorithm. Tracks are presented sequentially in the left window, and possible grain candidates are presented in the right window. The user can navigate through each frame and add or remove any grains to the track. Estimates for possible missing locations are presented based on the calculated trajectory. Units are in pixels in source images.

method, we are able to condense the 402 trajectories into 128, with 118 having at least 10 points and for which the average length is 54 points.

The acceleration due to the Lorentz force can now be calculated for each grain trajectory by applying a second order polynomial fit. The forces that dominate the motion of the grain here are the gravitational force $F_g = m\vec{g}$ and the Lorentz force due to the electric field, $F_E = q\vec{E}$. (Note that the string appears significantly angled away from vertical in our videos; this is due to the uneven floor in our laboratory but can be corrected.) We define \hat{h} to be the horizontal unit vector orthogonal to the direction of the gravity vector \vec{g} and parallel to the camera's focal plane. Calculating the angle ϕ_{vert} of the string from the vertical such that $\hat{g} \cdot \hat{E} = \sin(\phi_{vert})$, we find that the net force acting in the direction of \hat{h} is $F_h = ma_h = q\vec{E} \cdot \hat{h} = qE\cos(\phi_{vert})$.

To determine the quantity $\frac{q}{m}$ from this expression, we calculate the positions of each point in a trajectory along the \hat{h} basis vector. For each point in the trajectory, we calculate x_h , the normal distance of that point to the string center. This corrects for both the nonvertical gravitational vector and the camera's yaw and roll, which would otherwise introduce significant errors. We then apply a second order polynomial fit to the positions, with the known elapsed time $\Delta t = 10^{-3}$ s between each frame. The second-order coefficient a_{fit} is the acceleration orthogonal to gravity such that $ma_{fit} = qE\cos\phi_{vert}$. The root mean squared residual of this fit is denoted here as Δ_a and recorded for each trajectory.

C. Size determination

In order to use this experiment to measure charge segregation in arbitrary mixtures with continuous size distributions, it is not sufficient to roughly categorize grains as "large" or "small" based on a cursory analysis of the images, as is frequently done in other granular tribocharging experiments. Instead, we have developed a technique for estimating an individual grain's diameter from the images. The method we use assumes that the total light B reflected from a grain of diameter D onto the camera sensor is proportional to the grain's cross-sectional area. As our grains are nearly spherical and have diffusely reflective surfaces, this should provide a reasonably accurate estimate of the size. We can then determine the diameter D from the expression

$$D = C\sqrt{B} \quad (1)$$

for some empirically determined scaling constant C . The brightness B is found by summing the values of the pixels making up the grain in a particular image. The constant C is measured for each material by placing a sample of grains on a microscope slide, placing it in the experimental apparatus where the grains would be, and taking a high-speed video of the slide under normal operating lighting conditions. The slide is then examined under a microscope (see Fig. 4), where the actual spherical diameter of each grain can be determined. The background brightness, which has a mean pixel value of approximately 20–25, is subtracted out to give a mean-zero background level, and the pixel values in the vicinity of each grain are summed to determine B . We can then find the average value of $\frac{R}{\sqrt{B}}$ among all grains, which becomes our scaling constant C . The resulting size distribution is shown in Fig. 5.

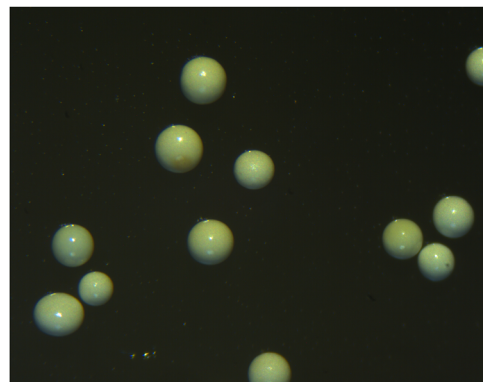


FIG. 4. Large size fraction of zirconia-silica grains (diameters 200 μm –300 μm) under a microscope. Grains are highly spherical with uniform smooth surfaces, with a few exceptions.

A major challenge we face is the prevalence of "motion blur" in our images. When filming these grains at 1000 frames/s, our camera has an exposure time of $\Delta t = 944 \mu\text{s}$. Some of our smaller grains can reach speeds that cause them to travel upwards of 20–30 pixels between frames in that time, causing them to appear elongated along their direction of motion. Our sizing method is resilient to blurring, as the window around each grain is large enough to include all photons reflected onto the sensor by the grain regardless of its speed or level of focus, but blurry grains do present a challenge for identifying and removing the nonzero-mean background.

1. Sizing procedure

First, we must remove noise from the image that originates from current leakage in the camera sensor. Known as "dark current," this is a function of the camera itself and can be found and

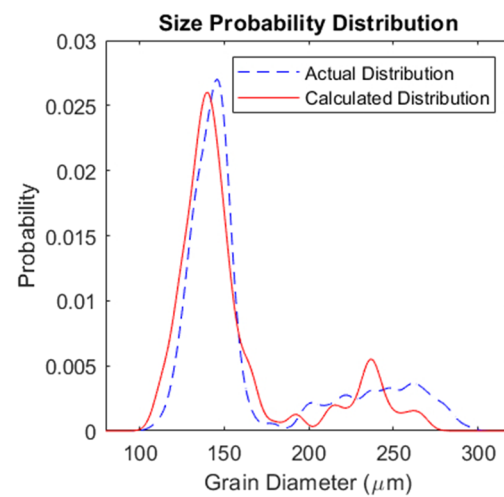


FIG. 5. Size distribution for equal mass (1:1) mixture of silica beads. Distribution obtained by measuring the distribution of each component separately and then calculating the mixture ratio from the known mass fractions.

corrected by taking a video without any illumination (e.g., with the lens cap on). The frames of the video are then averaged together on a pixel-by-pixel basis to create an average frame representing the dark current. This is then subtracted from each frame of our video. Next, we determine the mean remaining background pixel value and subtract it from the image. A mask is applied to each frame that selects only regions more than a standard diameter away from the string or any grain, and the mean value of these pixels is counted and removed from its frame as well.

We then determine an appropriate window around the grain in which its brightness is calculated. The width of this window is 1.5 standard diameters and is centered on the grain to be measured, ensuring that the entire grain is enclosed without being so large as to include other nearby objects. This subset image is then extracted such that the center of the subframe (x_s, y_s) is centered on the grain's location (x, y) in the frame. Next, we check that the grain fits within this window. We identify the trajectory to which the grain belongs and estimate its velocity $v = (\dot{x}, \dot{y})$ at the location in question. The grain's displacement is then calculated as $(\Delta x, \Delta y) = (\dot{x}\Delta t, \dot{y}\Delta t)$ pixels. If the dimensions of the window are not larger than this displacement plus a standard diameter, we cannot be sure we have fully captured the grain, and this location is rejected. Otherwise, sizing is done by summing the pixel values contained in the subframe and applying the conversion from that value B to the grain diameter D defined by Eq. (1).

Finally, because many of the grains are slightly out of focus or highly elongated, we manually compare the average diameter of each grain trajectory to the images of its positions. Some of these require manual correction, and some are too poorly resolved to be confident in the results obtained. After all grains have been confirmed, the results are saved and charge determination can begin.

To obtain an estimate for the uncertainty involved in this method, we return to the calibration images described in Sec. IV C. We apply this sizing algorithm to the images taken under experimental conditions, obtaining a set of diameter estimates D_{calc} . These values are then compared to the corresponding sizes as determined under microscopic analysis, and the root mean square residual is found for each size species. We have measured a root mean square residual for diameter measurements of $8.1 \mu\text{m}$ and $8.4 \mu\text{m}$ for small and large size species, respectively. Henceforth, we assume that each individual diameter measurement has an associated uncertainty of $\Delta_D = 8.4 \mu\text{m}$.

D. Calculation of grain charges

Given the measured grain size and grain acceleration, it is possible to derive the charge on an individual grain. From the grain's acceleration fit $a_{fit} = \frac{q}{m}$, the estimated diameter D_{est} , the material density ρ , and the electric field strength $E = \frac{V}{L}$, the charge q can be expressed as follows:

$$q = \frac{ma_{fit}}{E} = \frac{\pi\rho LD_{est}^3 a_{fit}}{6V}. \quad (2)$$

In this setup, we have applied a voltage of $V = 4 \text{ kV}$ to the parallel plates, with a spacing of $L = 60 \text{ mm}$ between them. These charge measurements are subject to a few significant sources of error, the largest of which by far are the uncertainties in a_{fit} and D_{est} . Here, we assume that these uncertainties are significantly larger than errors in

the applied voltage, which we have found to be accurate to less than 1% variation, and in the infinite parallel plate model for the electric field.

The uncertainty associated with the charge q can, therefore, be expressed as a combination of the uncertainties Δ_D and Δ_a as follows:

$$\Delta_q = q \sqrt{9 \left(\frac{\Delta_D}{D} \right)^2 + \left(\frac{\Delta_a}{a_{fit}} \right)^2}. \quad (3)$$

A sample plot of charge measurements is given in Fig. 6. Vertical error bars are given by the acceleration fit uncertainty Δ_a , and horizontal error bars are given by the sizing uncertainty Δ_D . These results include 128 trajectories collected from four camera drops. We have plotted the charge-to-mass ratio rather than the total charge as the former is determined from the acceleration a_{fit} and independent of the size measurements. Note that the large grains carry a negative charge, while the small grains are charged positively. This is a reversal from the trends observed in most previous experiments, where the smaller grains tend to charge negatively and the large are positive. This polarity reversal, with small grains charging positively, agrees with the predictions of our semianalytic model²⁹ and is consistent across experiments on different days and with different mixture ratios. We propose that this charging polarity was not observed in prior experiments due to contamination of prior experiments via atmospheric effects and/or charging other than grain-to-grain charging.

Although the tested size distribution is not entirely discrete, it is useful to examine these results in terms of large (greater than $200 \mu\text{m}$) and small (less than $200 \mu\text{m}$) grains. We observe that the small grains have a mean charge-to-mass ratio of $(3.22 \pm 2.64) \times 10^{-5} \text{ C/kg}$, whereas the large grains have a mean charge-to-mass ratio of $(-2.33 \pm 1.21) \times 10^{-5} \text{ C/kg}$. Including their calculated diameters and associated uncertainties, we find that the small grains have an average charge of $q_S = (1.17 \pm 1.09) \times 10^{-13} \text{ C}$ and the large grains have an average charge of $q_L = (-5.34 \pm 2.33) \times 10^{-13} \text{ C}$. Note that

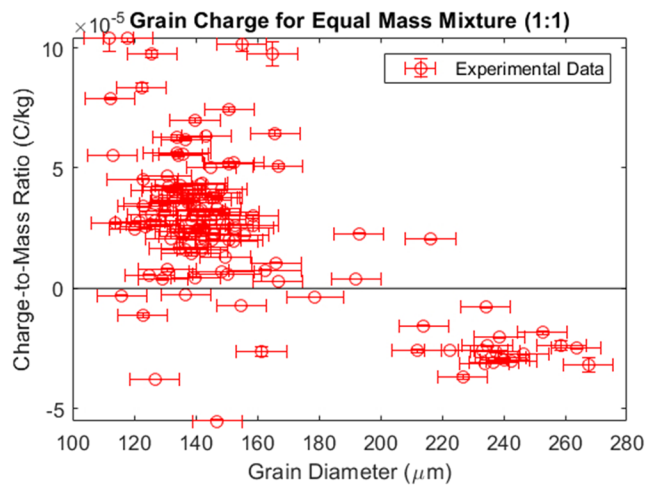


FIG. 6. Results of experimental analysis of the 1:1 (by mass) mixture of small (100–200 μm) and large (200–300 μm) spherical silica beads, with uncertainties due to acceleration (vertical) and diameter (horizontal) measurements shown.

the large error bounds on these values are only in part due to measurement uncertainties; granular tribocharging is a stochastic process that results in a wide spread in charge for a single species, as in Fig. 6, and this is reflected in the error bound on the mean charge.

To verify that this charging is due solely to grain-to-grain charge exchange occurring in vacuum, we have conducted tests using the same mixture and experimental conditions but without activating the shaker. In this experiment, we found that the small grains measured carried an average charge of $q_s(9.03 \pm 68.3) \times 10^{-15} \text{ C/kg}$ and the large grains carried an average charge of $q_L(-5.35 \pm 12.2) \times 10^{-14} \text{ C/kg}$. The mean charge on each species without shaking was at least an order of magnitude less than after shaking, suggesting that the majority of charge exchange does indeed occur in vacuum. We also note that the variance of the charge around the mean is significantly larger than the mean itself, indicating that there is little evidence of any significant correlation between size and charge polarity before shaking. We attribute the presence of what little charge is present to charge exchange during transport and preparation of the grains, but we remain confident that the dominant mechanism creating the charge segregation observed is granular tribocharging in vacuum.

V. CONCLUSIONS

This experimental methodology builds upon previous technology to measure tribocharging of a wide variety of granular mixtures under controlled environmental conditions. By conducting the entirety of the experiment in vacuum, this system reduces the effects of atmosphere and adsorbed water on the grain-to-grain charging process. These measurements provide not only the charge-to-mass ratio of a charged grain but also its approximate size and charge magnitude, without influencing the charge observed through the measurement process. For certain mixtures of more than one material, the images collected can even provide the capability to distinguish between materials with different reflective properties. We observe that silica grains charged solely in vacuum at approximately 30 μTorr exhibit a reversal of the charge polarity, as predicted by our model.²⁹

While this setup has proven capable of obtaining individual charge data in granular mixtures, there are areas for improvement, especially to the accuracy of the grain size measurements. Increasing the image resolution and illumination on the grains would likely improve sizing accuracy. Creating a compact test stand that can be placed entirely in our vacuum chamber limits the available space for lighting, but other solutions may exist that could greatly increase the signal-to-noise ratio. Additionally, further investigation is necessary to determine the degree to which any adsorbed water remains on the silica grains during charging and whether baking or another pre-treatment drying method is necessary before placing grains in the apparatus.

The reversal of grain charge polarity from that observed in prior experiments is a notable result that requires further study. It remains unclear whether this is due to the absence of significant atmosphere and/or water vapor, a result of physical or chemical differences in the size fractions, or some other unforeseen effect. Future experiments with grain sizes sieved out of a larger single fabrication batch, or with

other materials such as soda lime or borosilicate grains, may shed additional light on this phenomenon.

ACKNOWLEDGMENTS

The authors would like to thank Heinrich Jaeger, Victor Lee, and Scott Waitukaitis for their guidance and support in adapting this work from their high-speed videography experiment. This work was supported by a NASA Space Technology Research Fellowship (Grant No. NNX15AP69H). We thank Carlos Calle and his team at the Electrostatics and Surface Physics Laboratory (ESPL) at Kennedy Space Center's Swamp Works facility for their mentorship and guidance in designing the software controller and vacuum components of the experiment.

REFERENCES

- ¹T. Pahtz, H. Herrmann, and T. Shinbrot, *Nat. Phys.* **6**, 364 (2010).
- ²J. Kok and N. Renno, *Phys. Rev. Lett.* **100**, 014501 (2008).
- ³X. Zheng, N. Huang, and Y. Zhou, *J. Geophys. Res.: Atmos.* **108**, 4322, <https://doi.org/10.1029/2002jd002572> (2003).
- ⁴J. Gilbert, S. Lane, R. Sparks, and T. Koyaguchi, *Nature* **349**, 598 (1991).
- ⁵S. Liang, J. Zhang, and L. Fan, *Ind. Eng. Chem. Res.* **35**, 2748 (1996).
- ⁶G. Hendrickson, *Chem. Eng. Sci.* **61**, 1041 (2006).
- ⁷D. Saville, M. Al-Adel, and S. Sundaresan, *Ind. Eng. Chem. Res.* **41**, 6224 (2002).
- ⁸P. Cartwright, S. Singh, A. G. Bailey, and L. J. Rose, *IEEE Trans. Ind. Appl.* **IA-21**, 541 (1985).
- ⁹M. K. Mazumder, S. Banerjee, R. E. Ware, C. Mu, N. Kaya, and C. C. Huang, *IEEE Trans. Ind. Appl.* **30**, 365 (1994).
- ¹⁰D. J. Lacks and A. Levandovsky, *J. Electrost.* **65**, 107 (2006).
- ¹¹D. J. Lacks, N. Duff, and S. K. Kumar, *Phys. Rev. Lett.* **100**, 188305 (2008).
- ¹²K. M. Forward, D. J. Lacks, and R. M. Sankaran, *Phys. Rev. Lett.* **102**, 028001 (2009).
- ¹³J. Lowell and W. Truscott, *J. Phys. D: Appl. Phys.* **19**, 1273 (1986).
- ¹⁴J. Lowell and W. Truscott, *J. Phys. D: Appl. Phys.* **19**, 1281 (1986).
- ¹⁵S. Pence, V. Novotny, and A. Diaz, *Langmuir* **10**, 592 (1994).
- ¹⁶J. A. Wiles, M. Fialkowski, M. R. Radowski, G. M. Whitesides, and B. A. Gryzbowski, *J. Phys. Chem. B* **108**, 20296 (2004).
- ¹⁷Y. Zhang, T. Pahtz, Y. Liu, X. Wang, R. Zhang, Y. Shen, R. Ji, and B. Cai, *Phys. Rev. X* **5**, 011002 (2015).
- ¹⁸T. A. L. Burgo, T. R. D. Ducati, K. R. Francisco, K. J. Clinckspoor, F. Galembek, and S. E. Galembek, *Langmuir* **28**, 7407 (2012).
- ¹⁹K. M. Forward, D. J. Lacks, and R. M. Sankaran, *Ind. Eng. Chem. Res.* **48**, 2309 (2009).
- ²⁰K. M. Forward, D. J. Lacks, and R. M. Sankaran, *J. Electrost.* **67**, 178 (2009).
- ²¹H. Zhao, G. S. P. Castle, and I. I. Inculet, *J. Electrost.* **55**, 261 (2002).
- ²²H. Zhao, G. S. P. Castle, I. I. Inculet, and A. G. Bailey, *IEEE Trans. Ind. Appl.* **39**, 612 (2003).
- ²³S. R. Waitukaitis and H. M. Jaeger, *Rev. Sci. Instrum.* **84**, 025104 (2013).
- ²⁴S. R. Waitukaitis, V. Lee, J. M. Pierson, S. L. Forman, and H. M. Jaeger, *Phys. Rev. Lett.* **112**, 218001 (2014).
- ²⁵K. M. Forward, D. J. Lacks, and R. M. Sankaran, *J. Geophys. Res.: Space Phys.* **114**, A10109, <https://doi.org/10.1029/2009ja014559> (2009).
- ²⁶K. M. Forward, D. J. Lacks, and R. M. Sankaran, *Geophys. Res. Lett.* **36**, L13201, <https://doi.org/10.1029/2009gl038589> (2009).
- ²⁷T. Shinbrot, T. Komatsu, and Q. Zhao, *Europhys. Lett.* **83**, 24004 (2008).
- ²⁸J. C. Crocker and D. G. Grier, *J. Colloid Interface Sci.* **179**, 298 (1995).
- ²⁹D. Carter and C. M. Hartzell, *Phys. Rev. E* **95**, 012901 (2017).